Natural Hazards
https://doi.org/10.1007/s11069-023-05975-2

ORIGINAL PAPER

Storm surge predictions from ocean to subgrid scales

Johnathan Woodruff[1] · J. C. Dietrich[1] · D. Wirasaet[2] · A. B. Kennedy[2] · D. Bolster[2]

Received: 25 October 2022 / Accepted: 30 March 2023

Abstract

The inland propagation of storm surge caused by tropical cyclones depends on large and small waterways to connect the open ocean to inland bays, estuaries, and floodplains. Numerical models for storm surge require these waterways and their surrounding topography to be resolved sufficiently, which can require millions of computational cells for flooding simulations on a large (ocean scale) computational domain, leading to higher demands for computational resources and longer wall-clock times for simulations. Alternatively, the governing shallow water equations can be modified to introduce subgrid corrections that allow coarser and cheaper simulations with comparable accuracy. In this study, subgrid corrections are extended for the first time to simulations at the ocean scale. Higher-level corrections are included for bottom friction and advection, and look-up tables are optimized for large model domains. Via simulations of tides, storm surge, and coastal flooding due to Hurricane Matthew in 2016, the improvements in water level prediction accuracy due to subgrid corrections are evaluated at 218 observation locations throughout 1500 km of coast along the South Atlantic Bight. The accuracy of the subgrid model with relatively coarse spatial resolution (E_{RMS} = 0.41 m) is better than that of a conventional model with relatively fine spatial resolution (E_{RMS} = 0.67 m). By running on the coarsened subgrid model, we improved the accuracy over efficiency curve for the model, and as a result, the computational expense of the simulation was decreased by a factor of 13.

Keywords Hurricane · Coastal flooding · South Atlantic Bight · ADCIRC

✉ Johnathan Woodruff
jlwoodr3@ncsu.edu

J. C. Dietrich
jcdietri@ncsu.edu

D. Wirasaet
dwirasae@nd.edu

A. B. Kennedy
akenned4@nd.edu

D. Bolster
dbolster@nd.edu

1 Department of Civil, Construction, and Environmental Engineering, North Carolina State University, 915 Partners Way, Raleigh, NC 27695, USA

2 Department of Civil and Environmental Engineering and Earth Science, University of Notre Dame, 156 Fitzpatrick Hall of Engineering, South Bend, IN 46556, USA

Published online: 05 May 2023

1 Introduction

Tropical cyclones and other coastal storms can cause storm surge, which is the rise in water levels above the normal astronomical tides (Harris 1963). Storm surge can damage infrastructure along the coast and far inland (Lin et al. 2010a; Tomiczek et al. 2014; Needham et al. 2015). The extent to which storm surge can propagate overland depends on topographic and bathymetric controls, including natural and built channels and barriers, as well as varying friction associated with land cover (Stark et al. 2015; Herdman et al. 2018). Storm surge and flooding can be predicted with computational models generally based on the numerical solution of 2D shallow water equations (Westerink et al. 2008; Lin et al. 2010b; Leijnse et al. 2021). The computational model can generate detailed maps of inundation levels and extents, which are used to support decision making for coastal communities (Xian et al. 2015; Ramirez et al. 2016; Rucker et al. 2021). Therefore, during a storm event, it is essential that model predictions are the best possible representation of flooding in coastal regions.

Storm surge models are applied typically along large stretches of coastline, to predict water levels, currents, and flooding extents in the full region affected by the storm. These models represent the coastal environment with numerical grids (or meshes) with varying spatial resolution—often finer near the coast, where the bathymetry/topography varies significantly and predictive accuracy is critical. The Sea, Land, and Overland Surges from Hurricanes (SLOSH) model (Jelesnianski et al. 1992) resolves length scales on the order of hundreds of meters and includes limited topographical complexity (Zhang et al. 2008). The ADvanced CIRCulation (ADCIRC) model (Luettich et al. 1992; Westerink et al. 2008) uses finite-element meshes with small length scales on the order of tens of meters to represent hydraulic and topographic information with high fidelity (Bunya et al. 2010; Hope et al. 2013). Typically, the inclusion of more geospatial information allows for more accurate flooding predictions, because the model can represent flows at very small scales (Bilskie and Hagen 2013; Kerr et al. 2013). However, such inclusion can lead to a model with a large number of grid cells that is too computationally expensive to obtain results in a timely manner. In addition, due to technologies like light detection and ranging (LiDAR), there will be a gap between any model and the best-available representation of the coastal environment (e.g., digital elevation models (DEMs) with spatial resolutions less than 1 m) (Danielson et al. 2018). Traditionally, trade-offs between spatial accuracy and computational efficiency must be considered when developing a model.

Subgrid corrections can bridge the gap between model and finer scales. The governing shallow water equations are averaged (Defina 2000) to introduce closure terms, which can include higher-resolution data to correct flow variables (flow accelerations, water levels, and current velocities) at the grid scale. Bates and Hervouet (1999) used subgrid corrections to improve predictions of the moving wet/dry boundary. Defina (2000) applied corrections to the convective accelerations to incorporate small-scale changes in flow due to ground irregularities. Volp et al. (2013) corrected bottom friction to account for variable bathymetry and roughness by assuming uniform flow direction and constant friction slope. These and other studies aim to attain highly accurate results on grids with length scales that are several orders of magnitude larger than those of the topographic datasets (Casulli and Stelling 2011).

Subgrid corrections have only recently been used for storm surge predictions. Sehili et al. (2014) incorporated winds and storm surge into a regional Unstructured Tidal, Residual, Intertidal Mudflat ($UnTRIM^2$) subgrid model of the North Sea. Daily meteorological predictions were used to force an operational subgrid model of the Elbe Estuary to predict water levels, velocities, and salinity transport. They achieved accurate predictions with the subgrid model while decreasing computational expense by a factor of 20. Wang et al. (2014) used the ocean-scale Semi-implicit Eulerian Lagrangian Finite Element (SELFE) hurricane storm surge model to provide water levels to UnTRIM^2 to predict water levels in New York City during Hurricane Sandy in 2012. High-resolution elevation data were used to predict street-scale water levels comparable to observations taken during the storm. Woodruff et al. (2021) added subgrid corrections into ADCIRC with real hurricane winds and storm surge forcing. Using a relatively small domain focused near the landfall location of Hurricane Rita in 2005, which caused extensive flooding in southwest Louisiana, the authors obtained accurate results while running ADCIRC with subgrid corrections on a coarse computational mesh that decreased run time by a factor of 32 when compared to a high-resolution counterpart that had nearly 40 times more grid cells.

There are remaining challenges to the implementation of subgrid corrections for storm surge simulations on large domains. One challenge is to account for small-scale variations in bottom roughness and advection, which can significantly affect predicted water depths during a storm (Rego and Li 2010). Bottom friction is the primary contributor to storm surge attenuation as it flows overland (Resio and Westerink 2008), and small uncertainties in bottom friction can lead to large errors in predicted surge elevations (Akbar et al. 2017). The averaging of topographic and bathymetric features can lead to over-estimations of bottom friction (Defina 2000; Volp et al. 2013; Kennedy et al. 2019), which may inhibit propagation. Advection, due to storm surge interaction with the astronomical tides and shelf geometry, can affect predicted water levels by as much as 1 m in some locations (Thomas et al. 2019). However, when averaging to larger grid-scale areas, subgrid models may not represent small-scale variations in nonlinear advection in complex coastal environments (Defina 2000; Kennedy et al. 2019).

Another challenge is that most previous subgrid studies have focused on demonstrating the performance of the approach on small regional domains (Roig 1994; Bates and Hervouet 1999; Defina 2000; Wu et al. 2016; Kennedy et al. 2019) with areas less than 500 km^2. However, for storm surge applications, small domains can lead to significant underpredictions and undue boundary influences (Blain et al. 1994; Pringle et al. 2018). Larger domains are necessary to represent the storm's effects in open water, its interactions with the complex coastal environment, and the development of surge forerunners and shelf edge waves (Westerink et al. 1994). Because of their relatively high number of grid cells, large, ocean-scale hydrodynamic models require high-performance computing (HPC) systems and parallelized coding practices to reduce computing times (Tanaka et al. 2011; Roberts et al. 2021).

The ability of subgrid models to be parallelized and scaled to large domains, the availability of high-resolution data, and data processing limitations have been contributing factors to why previous research studies have not applied subgrid models to larger domains. In this study, we investigate the extension of subgrid models for storm surge on ocean-scale domains. It is hypothesized that accurate predictions of storm surge at the smallest coastal scales can be obtained if: (1) higher-level subgrid corrections to bottom friction and advection are implemented into a widely used storm surge model, (2) the extensive datasets needed to describe subgrid information can be efficiently processed, and (3) storm surge predictions are corrected for flows in complex coastal environments. We extend subgrid corrections in ADCIRC and comprehensively evaluate their performance compared to conventional methodologies. First, we introduce higher-level corrections to advection and bottom friction and demonstrate their benefits for controlled flow on a synthetic domain. Then, we extend to a domain of the Western North Atlantic Ocean, to simulate the storm surge generated by Matthew in 2016. This ocean-scale model will use hundreds of DEMs and land cover datasets to represent coastal regions from south Florida to the North Carolina Outer Banks. Finally, by comparing with observations from the storm, we demonstrate improvements in the subgrid model's ability to predict water levels over a range of spatial scales along the coast.

2 Methods

2.1 Extension of subgrid corrections in ADCIRC

2.1.1 Closures for bottom friction and advection

ADCIRC is a coastal circulation model with applications in predictions of tides (Luettich et al. 1992; Westerink et al. 1992; Blain et al. 1998), density-driven circulation (Dresback et al. 2010; Blain et al. 2012; Cyriac et al. 2020), and storm surge (Westerink et al. 2008; Bunya et al. 2010; Dietrich et al. 2010; Weaver and Luettich 2010; Sebastian et al. 2014). ADCIRC uses the continuous-Galerkin, finite-element method to solve shallow water equations that consist of the depth-integrated mass equation reformulated into the Generalized Wave Continuity Equation (GWCE) and conservative momentum equations to predict water levels and current velocities at vertices in an unstructured mesh. Using volume-averaging techniques from Whitacker (1999), these equations were averaged to obtain the subgrid system for locally averaged flow variables. Such a system (see the full detailed derivation in Woodruff et al. 2021) consists of the averaged momentum equations:

$$
\begin{aligned}
\frac{\partial \langle UH \rangle_G}{\partial t} + g C_\zeta \langle H \rangle_G \frac{\partial \langle \zeta \rangle_W}{\partial x} = &- \frac{\partial C_{UU} \langle U \rangle \langle UH \rangle_G}{\partial x} - \frac{\partial C_{VU} \langle V \rangle \langle UH \rangle_G}{\partial y} \\
&- f \langle VH \rangle_G - g \langle H \rangle_G \frac{\partial P_A}{\partial x} + \phi \left\langle \frac{\tau_{sx}}{\rho_0} \right\rangle_W - \frac{C_{M,f} \langle \mathbf{U} \rangle \langle UH \rangle_G}{\langle H \rangle_W} \\
&+ \frac{\partial}{\partial x} E_h \frac{\partial \langle UH \rangle_G}{\partial x} + \frac{\partial}{\partial y} E_h \frac{\partial \langle UH \rangle_G}{\partial y},
\end{aligned}
\tag{1}
$$

and:

$$
\begin{aligned}
\frac{\partial \langle VH \rangle_G}{\partial t} + g C_\zeta \langle H \rangle_G \frac{\partial \langle \zeta \rangle_W}{\partial y} = &- \frac{\partial C_{UV} \langle U \rangle \langle VH \rangle_G}{\partial x} - \frac{\partial C_{VV} \langle V \rangle \langle VH \rangle_G}{\partial y} \\
&- f \langle UH \rangle_G - g \langle H \rangle_G \frac{\partial P_A}{\partial y} + \phi \left\langle \frac{\tau_{sy}}{\rho_0} \right\rangle_W - \frac{C_{M,f} \langle \mathbf{U} \rangle \langle VH \rangle_G}{\langle H \rangle_W} \\
&+ \frac{\partial}{\partial x} E_h \frac{\partial \langle VH \rangle_G}{\partial x} + \frac{\partial}{\partial y} E_h \frac{\partial \langle VH \rangle_G}{\partial y},
\end{aligned}
\tag{2}
$$

and the averaged GWCE:

$$\begin{aligned}
&\phi\frac{\partial^2\langle\zeta\rangle_W}{\partial t^2}+\frac{\partial\phi}{\partial t}\frac{\partial\langle\zeta\rangle_W}{\partial t}+\tau_0\phi\frac{\partial\langle\zeta\rangle_W}{\partial t}\\
&\quad-\frac{\partial}{\partial x}\left(g\langle H\rangle_G\frac{\partial\langle\zeta\rangle_W}{\partial x}\right)-\frac{\partial}{\partial y}\left(g\langle H\rangle_G\frac{\partial\langle\zeta\rangle_W}{\partial y}\right)\\
&\quad+\frac{\partial\langle\tilde{J}_x\rangle_G}{\partial x}+\frac{\partial\langle\tilde{J}_y\rangle_G}{\partial y}-\langle UH\rangle_G\frac{\partial\tau_0}{\partial x}-\langle VH\rangle_G\frac{\partial\tau_0}{\partial y}=0,
\end{aligned}\tag{3}$$

where

$$\langle\tilde{J}_x\rangle_G=\text{RHS of (1)}+\tau_0\langle UH\rangle_G\quad\text{and}\quad\langle\tilde{J}_y\rangle_G=\text{RHS of (2)}+\tau_0\langle VH\rangle_G.$$

In the above equations, $\langle s\rangle_G$ and $\langle s\rangle_W$ denotes the grid-average and wet-average, respectively, of the flow variables s ($s = H, UH, VH, \zeta$), and $\phi(\langle\zeta\rangle_W)$ is the wet area fraction, U and V are the water velocities in the x and y directions, $H = \zeta + h$ is the water depth, ζ is the water surface elevation, h is the bathymetric depth, f is the Coriolis parameter, g is the acceleration due to gravity, P_A is the atmospheric pressure, τ_{sx} and τ_{sy} are surface stresses, E_h is the lateral stress coefficient, τ_0 is a positive (spatially varying) parameter weighting the primitive continuity equation. The unknown solution variables to be computed are the surface elevation $\langle\zeta\rangle_W$ and the averaged x- and y- directed flux per unit width $\langle UH\rangle_G$, $\langle VH\rangle_G$. The grid-averaged water depth $\langle H\rangle_G$, wet-averaged water depth $\langle H\rangle_W$, and wet fraction ϕ are found using look-up tables (as elaborated below) for a given surface elevation $\langle\zeta\rangle_W$. The grid-scale velocity $\langle \boldsymbol{U}\rangle$ corresponds to the ratio $\langle \boldsymbol{UH}\rangle_G/\langle H\rangle_G$.

Several closure coefficients are introduced by the averaging and are indicated in red font in Eqs. 1, 2, and 3. These closure coefficients include: the convective acceleration coefficients C_{UU}, C_{VU}, C_{UV}, and C_{VV}; the friction coefficient $C_{M,f}$; and the water surface gradient coefficient C_ζ. To only apply corrections to the wetting and drying (denoted a ‘Level 0’ correction by Kennedy et al. 2019), these closure terms would be represented as the following:

$$C_{UU}, C_{VU}, C_{UV}, C_{VV} = 1, \qquad C_{M,f} = \left\langle \frac{gn^2}{H^{1/3}} \right\rangle_W, \qquad C_\zeta = 1, \tag{4}$$

where n is a Manning’s roughness coefficient, assigned typically from land-use/landcover data sets.

In this work, we retain the water surface gradient correction as $C_\zeta = 1$, but we extend corrections for the advection and bottom friction coefficients (denoted as ‘Level 1’ corrections by Kennedy et al. 2019). For the bottom friction, Volp et al. (2013) created a weighted friction coefficient by applying the conveyance method, which was generalized for a two-dimensional setting by assuming uniform flow direction and friction slope at the subgrid level across a coarsened computational cell. This flow assumption results in the correction factor adjusting the conventional friction coefficient as follows (Kennedy et al. 2019):

$$C_{M,f} = \langle H\rangle_W R_v^2 \quad \text{where:} \quad R_v = \frac{\langle H\rangle_W}{\left\langle H^{3/2} C_f^{-1/2}\right\rangle_W}, \tag{5}$$

where the dimensionless friction coefficient C_f is calculated using Manning’s equation:

$$C_f = \frac{gn^2}{H^{1/3}}. \tag{6}$$

In addition, the above mentioned canonical flow assumption at the subgrid level leads to the following advection correction coefficients (Defina 2000; Kennedy et al. 2019):

$$C_{UU} = C_{VU} = C_{UV} = C_{VV} = \frac{1}{\langle H \rangle_W} \left\langle \frac{H^2}{C_f} \right\rangle_W R_v^2. \tag{7}$$

Note that the equations (5) and (7) depend only on subgrid water depth and bottom roughness. Therefore, these coefficients can be pre-computed for a range of surface elevation values and stored as look-up tables. With the look-up table, evaluating these coefficients can be done efficiently and is independent of the subgrid resolution, as the procedure reduces to retrieving relevant entries in the look-up tables and requires only $O(1)$ operations.

2.1.2 Wetting and drying

The conventional ADCIRC requires extensive logic to determine whether an element or vertex is considered 'wet' (included in the computations) or 'dry' (ignored) (Dietrich et al. 2004; Medeiros and Hagen 2013). This algorithm requires elements and vertices to be either fully wet or fully dry (i.e., to be wet, a triangular element must have nonzero water depths at all three of its vertices). Logic decisions are based on local water depths, water surface gradients, and bottom friction. ADCIRC's wet/dry algorithm has been applied for accurate predictions of flooding in many overland regions (e.g., Westerink et al. 2008; Hope et al. 2013; Thomas et al. 2019). However, this approach can lead to inaccuracies in the location of the wet/dry interface (Rucker et al. 2021), which can be represented only at the grid scale, and to numerical instabilities, partly due to the addition/subtraction of entire elements to the local conservation of mass and momentum.

In subgrid ADCIRC, an alternative wetting and drying algorithm was devised. The algorithm is based solely on the local wet area fraction (Woodruff et al. 2021); more specifically, mesh quantities (elements and vertices) are considered wet if they satisfy the one condition:

$$\phi > \phi_{\min} \tag{8}$$

where ϕ_{min} is a minimum wet area fraction set by the user. Typical values for $\phi_{\min}$ are in the range of 0.01 to 0.1. This setting allows for partially wet elements and vertices, thus smoothing the transition between the active and inactive parts of the domain.

In previous subgrid studies with a similar wetting criterion (Defina 2000; Casulli and Stelling 2011; Wang et al. 2014; Kennedy et al. 2019; Woodruff et al. 2021), one challenge has been the inability of the subgrid model to block flow between hydraulically disconnected regions. This is a result of assuming that flow variables are constant over their respective regions (Casulli 2019). Therefore, where a coarsened computational element spans a raised feature (e.g., dune, levee, or barrier island) between two water bodies, the coarsened subgrid model would not be able to "see" that these two water bodies are not hydraulically connected. One solution is to incorporate cell clones that predetermine connectivity between computational cells (Casulli 2019; Begmohammadi et al. 2021); however, this solution cannot be implemented readily in ADCIRC because of its vertex-based numerical scheme. Cell clones rely on pre-computing flow across cell edges, instead of along them as is done in ADCIRC. Thus, the addition of cell clones to ADCIRC is left for future work.

Instead, to prevent flows across small barriers, we allow the wetting criterion $\phi_{\min}$ to vary spatially. In most of the domain, it retains its typically small values, thus allowing computations in areas that are barely wet. However, in areas that include a dune crest, levee, or barrier island (Fig. 1), the criterion can be set to higher values, thus preventing flows until the water level in these areas reaches an elevation sufficient for over-topping. These areas are identified manually before the simulation based on high points in the topography, and the higher $\phi_{\min}$ values are specified for select vertices and elements. In practice, this can be done relatively quickly by using a polygon shapefile that outlines the areas where variable ϕ_{min} is desired. From there, a simple Python script can be used to identify and store the elements and vertices contained in the polygon to be looked up later when ADCIRC is running. Herein, we use a value of $\phi_{\min} = 0.05$ in most of the domain, and a higher value of $\phi_{\min} = 0.99$ in select areas to represent flow barriers.

2.1.3 Precomputing corrections at the grid scale

ADCIRC uses the continuous-Galerkin, finite-element method to solve for water levels and current velocities at the vertices of triangular finite elements within an unstructured mesh. Accordingly, subgrid corrections are included by averaging quantities over areas corresponding to the elements and vertices (Woodruff et al. 2021). Element-averaged quantities include: $\langle H \rangle_G$, C_{UU}, C_{VU}, C_{UV}, C_{VV}, and ϕ, whereas vertex-averaged quantities include: $\langle H \rangle_G$, $\langle H \rangle_W$, $C_{M,f}$, and ϕ. These averaged quantities are computed from elevation and land-cover raster datasets at a much higher resolution than the model grid. Note that $\langle H \rangle_G$ and ϕ must be represented as both vertex- and element-averaged quantities, due to how ADCIRC uses these variables to solve the governing shallow water equations.

For the element-averaged quantities, each element is split into three sub-elements (Fig. 2), the raster cells within each sub-element area are located, and then the averaged quantities are computed for a given water surface elevation. For vertex-averaged quantities, the values from the surrounding element sub-areas are integrated and area-averaged to the vertex. Additionally, depending on the closure approximation used for each term in the governing-equation, either a grid-averaged $\langle \cdot \rangle_G$ or a wet-averaged representation $\langle \cdot \rangle_W$ was computed. For grid-averaged quantities, the entire averaging area is taken into account,

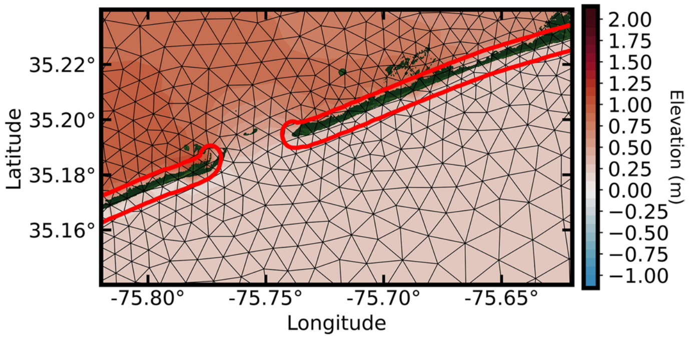

Fig. 1 Water level contours (m relative to NAVD88) along the North Carolina Outer Banks during a simulation of Hurricane Matthew in 2016 on the SABv2 mesh. The barrier islands, where the wetting criterion $\phi_{\min} = 0.99$ has a higher value, are outlined in red

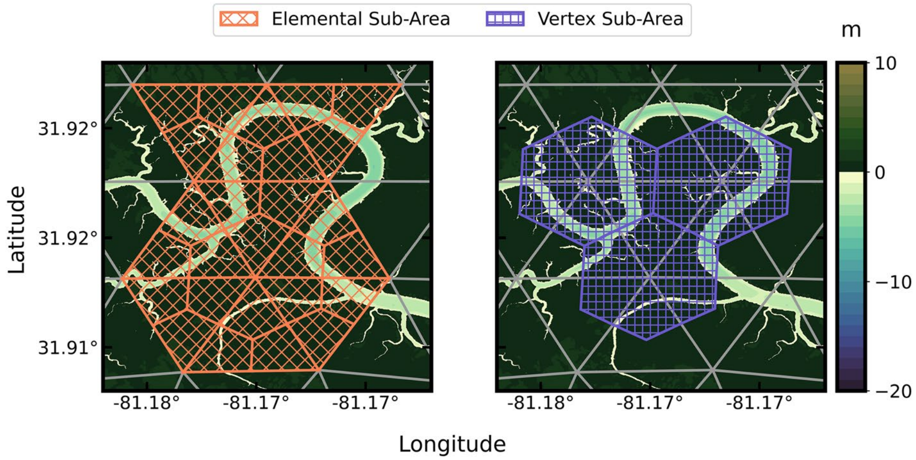

Fig. 2 Examples of element- and vertex-averaged areas: (left) averaged quantities from sub-elements are combined for each triangular element, and (right) averaged quantities from sub-elements are combined for each vertex for a tidal creek near Savannah, GA

whereas for wet-averaged quantities, only the subgrid areas that are underwater for a particular water surface elevation are included.

For computational efficiency, we use look-up tables in subgrid models while performing calculations. These tables are created by pre-computing subgrid quantities prior to the start of the simulation using information from bathymetric and landcover datasets. Upon initiation of the model, these arrays are read into memory to be accessed by the code for the duration of a simulation. In Woodruff et al. (2021), for element-based quantities, the size of the look-up table of each quantity was:

$$N_{\zeta} \times N_{\mathrm{VE}} \times N_{\mathrm{E}}, \tag{9}$$

where N_{ζ} is the number of water surface elevations used in the look-up table (e.g., 401 possible elevations between −20 m and +20 m), $N_{\mathrm{VE}} = 3$ is the number of vertices in a triangular element, and N_{E} is the number of elements in a computational mesh. For vertex-based quantities, the size of the look-up table is:

$$N_{\zeta} \times N_{V}, \tag{10}$$

where N_V is the number of vertices in a mesh.

Although look-up tables are used commonly to support subgrid corrections (Sehili et al. 2014; Wu et al. 2016; Kennedy et al. 2019; Woodruff et al. 2021; Begmohammadi et al. 2021), their expansion to ocean-scale domains created challenges for both their creation and their use at runtime. For the precomputations to create the look-up table in this study, the in-memory data storage of ocean-scale elevation and landcover data was managed carefully. The creation of the subgrid look-up tables was done entirely in Python (https://github.com/ccht-ncsu/subgridADCIRCUtility). Although datasets were split into manageable sizes, the task is challenging with CPUs because relatively small (0.25° × 0.25°) DEM tiles with 1/9 arc-second resolution contain almost 66 million pixels. To speed up the calculations, within the coverage of the datasets, subgrid calculations were performed using a Graphical Processing Unit (GPU) accelerated Python library called CuPy (Ryosuke et al.

2017), by looping through each of the elevation and landcover datasets. Outside the coverage of the datasets (e.g., in open water), the look-up tables were constructed to mimic the conventional ADCIRC, by allowing elements and vertices to be either fully wet or fully dry. These look-up tables were then saved in a NetCDF-formatted file to be read by subgrid ADCIRC.

For the new mesh described below, the NetCDF-formatted file would have been larger than 10 GB, which has implications for file input and memory usage at runtime. For meshes with higher resolution, the look-up table sizes would become untenable. To reduce their sizes, the look-up tables were changed to consider a set of possible ϕ values, representing a state of dryness ($\phi = 0$) to fully wet ($\phi = 1$) at an evenly spaced increment. Averaged variables were then calculated by using the water surface elevations that would correspond to these wet area fractions. This reduced the size of the look-up tables to:

$$N_{\phi} \times N_{VE} \times N_{E} \tag{11}$$

where N_{ϕ} is the number of possible ϕ values, which is determined by the user. This is contrasted with the number of possible surface elevations, N_{ζ}, in the earlier version of the look-up tables in Eq. 9. Whereas N_{ζ} was set typically to larger values (e.g., 401 possible water surface elevations), N_{ϕ} can be set to smaller values and still represent the variability in wet area fraction at each location. Herein, we use $N_{\phi} = 11$, which decreased the look-up table size. With this new scheme, a new look-up table of N_{ϕ} water surface elevations (ζ) corresponding to each ϕ increment was derived so that the ϕ for a particular element could be found depending on the water surface elevation in the element, the ζ look-up table, and the evenly spaced ϕ increments.

2.2 Storm simulations with subgrid corrections

2.2.1 South Atlantic Bight

Subgrid ADCIRC is extended for storm surge predictions along the South Atlantic Bight (SAB) on the southeast US coast. This region stretches from West Palm Beach, Florida (FL), to Cape Hatteras, North Carolina (NC), and includes more than 1000 km of coastline with a maximum shelf width of 200 km (Atkinson and Menzel 1985). The SAB's location and wide continental shelf make it particularly vulnerable to storm surge caused by tropical cyclones. Many studies have sought to understand the complex behavior of tides and circulation in this region (e.g., Redfield 1958; Blumberg and Mellor 1983; Chen et al. 1999). Tidal prediction along the SAB is particularly challenging due to the amplification that occurs as the tide propagates from the shelf break toward the coast, and due to the dramatic dissipation in energy as it interacts with the complex estuarian and riverine geometry present in the region (Blanton et al. 2004; Bacopoulos and Hagen 2017).

Due to the large size of the SAB, a substantial amount of elevation and landcover data are available to describe its coastline. A total of 830 elevation and landcover datasets (415 of each) were identified for use in this study (Fig. 3). Elevation datasets were collected from the National Oceanic and Atmospheric Administration (NOAA) through the NOAA Digital Coast platform, and from The National Map (TNM) from the United States Geological Survey (USGS). The NOAA datasets are comprised of $1/9$ arc-second and $1/3$ arc-second digital elevation model (DEM) tiles of nearshore bathymetry and topography from the continuously updated digital elevation model (CUDEM) produced by the NOAA National Centers for Environmental Information (CIRES 2014). These datasets

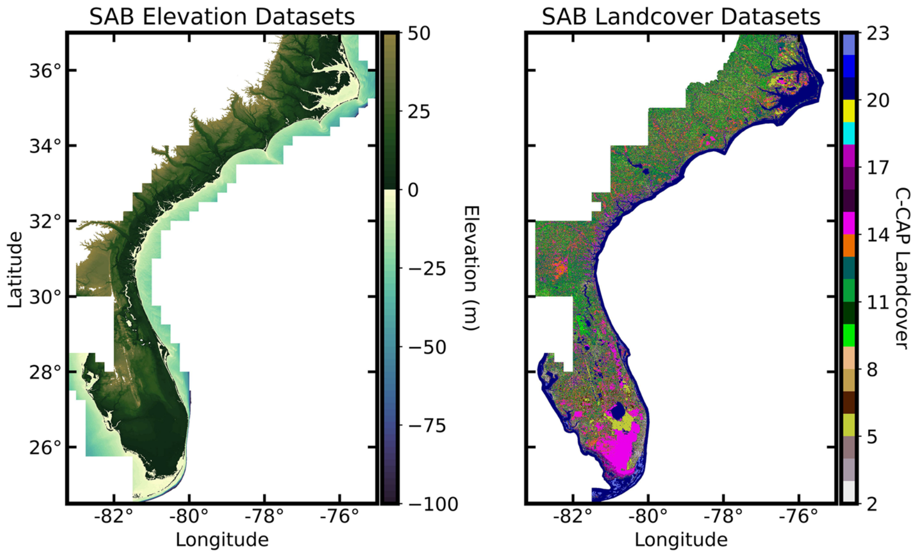

Fig. 3 Merged rasters containing the 415 elevation and 415 landcover datasets for the SAB

were merged using QGIS with 1/3 arc-second DEM tiles from TNM for inland regions. Land-use and landcover are represented by Coastal Change Analysis Program (C-CAP) regional 1 arc-second resolution datasets. It should be noted that, although the model domain will extend beyond the SAB to also represent the western North Atlantic Ocean, Caribbean Sea, and Gulf of Mexico, subgrid corrections were applied only to the SAB region where flooding is expected and where detailed water level analysis is desired. This reduced the overall amount of data, but even so, these elevation and landcover datasets amounted to more than 197 GB of compressed raster-formatted data.

2.2.2 Mesh development

Several meshes have been developed for ADCIRC-related studies in the SAB. Blanton and Luettich (2008) created a high-fidelity mesh to resolve important topographic and bathymetric features in North Carolina and extended the mesh inland to the 15 m contour. A mesh with high resolution along the South Carolina coast was developed to resolve features with the size on the order of 100 m (URS Corporation 2009). Bender (2013, 2014, 2015) developed meshes to cover the region from South Florida to Georgia. These meshes were used to develop storm surge and flooding risk maps for their areas of coverage. Thomas et al. (2022) merged these regional meshes to describe the entire SAB with a mesh with about 5.5 million vertices and an average resolution in coastal areas of about 100 m. Apart from high-resolution mesh development for the use in floodplain mapping studies, coarser meshes like the Hurricane Storm Surge Operational Forecast System (HSSOFS) mesh are used during active storm events to forecast water levels along a coast. The HSSOFS mesh consists of about 1.8 million vertices, has an average resolution in coastal areas of about 500 m, with floodplain coverage from Southern Texas along the Gulf of Mexico to the North Carolina Outer Banks (Riverside Technology and AECOM 2015).

Recently, a mesh was developed as part of the South Atlantic Coastal Study (SACS; U.S. Army Corps of Engineers 2021), with the goal to understand vulnerability and flooding risks along the entire coastline. The SACS mesh has a minimum element edge length of about 20 m, and thus, it resolves most of the hydraulically significant channels along the SAB. This mesh was validated for seven historical storms and then used in a study involving ensembles of thousands of synthetic storms (Owensby et al. 2020). However, the SACS mesh is expensive, with 12, 288, 247 elements and 6, 179, 416 vertices. Although this mesh is the state-of-the-art for storm surge predictions in the SAB, there is an opportunity for subgrid corrections to offer comparable accuracy on a coarser (more-efficient) mesh.

In this study, a new mesh was developed to test subgrid corrections for storm surge predictions in the SAB. This mesh provides coverage at ocean scales but with relatively coarse resolution along the SAB. It consists of 772, 268 elements and 392, 358 vertices, with a maximum element edge length of 50 km in open water and a minimum of 500 m in the nearshore. These maximum and minimum resolutions were chosen so the mesh would resolve large-scale channels and bathymetric features, but would alias many subgrid-scale features like small tidal channels, raised roadways, or intercoastal waterways at the grid level. Elements and vertices were aligned with a high-resolution coastline along the SAB (Contreras et al. 2021) and the US medium shoreline (National Oceanic and Atmospheric Administration 2021b) in other regions. The mesh was bounded at the same inland locations as the SACS mesh, which has an inland boundary that aligns with either the 10 m or 20 m topographical contour (Owensby et al. 2020). Thalweg data were used to align elements and vertices with important hydraulic features like major rivers, inlets, and inland waterways. Steep bathymetric gradients in the offshore were resolved to ensure proper tidal propagation (Roberts et al. 2019b). The mesh was designed using Oceanmesh2D (Roberts et al. 2019a). It should be noted that this new SABv2 mesh has 15 times fewer computational grid cells than the existing SACS mesh. The highest disparities in resolution between the two meshes occur at inland locations along the complex coastline of the SAB (Fig. 4).

2.2.3 Hurricane Matthew in 2016

Hurricane Matthew evolved in the western North Atlantic Ocean over a 15-day period during 2016. The storm started as a strong tropical wave below 10° N latitude on September 23 off the western coast of Africa, and strengthened during the next few days until it became a tropical storm on September 28 just north of Barbados in the Lesser Antilles of the West Indies (Stewart 2017). Matthew rapidly intensified between September 30 and October 1 to a category-5 hurricane on the Saffir-Simpson scale with a peak intensity of 145 knots. During the eye wall replacement cycle, Matthew downgraded to a category 4 storm before making landfall near Les Anglais, Haiti, on October 4. Matthew weakened as it passed through the Bahamas, making landfall near West End on Grand Bahama Island on October 7 with category-3 status. Continuing northward, the storm ran shore-parallel between 30 and 50 nautical miles from Florida to North Carolina with category 2 and 1 intensity before starting its extra-tropical transition on October 9, moving eastward of Cape Hatteras, North Carolina, and dissipating in the North Atlantic (Stewart 2017).

The storm's effects on coastal water levels were observed by a total of 232 temporary gauges and long-term stations throughout the SAB. NOAA operates 22 stations, typically at the open coast. The USGS deployed 204 temporary gauges both at the coast and along inland waterways, and the Flood Inundation Mapping and Alert Network (FIMAN) operated 6 permanent stream gauges during the event (Fig. 5). These observations describe

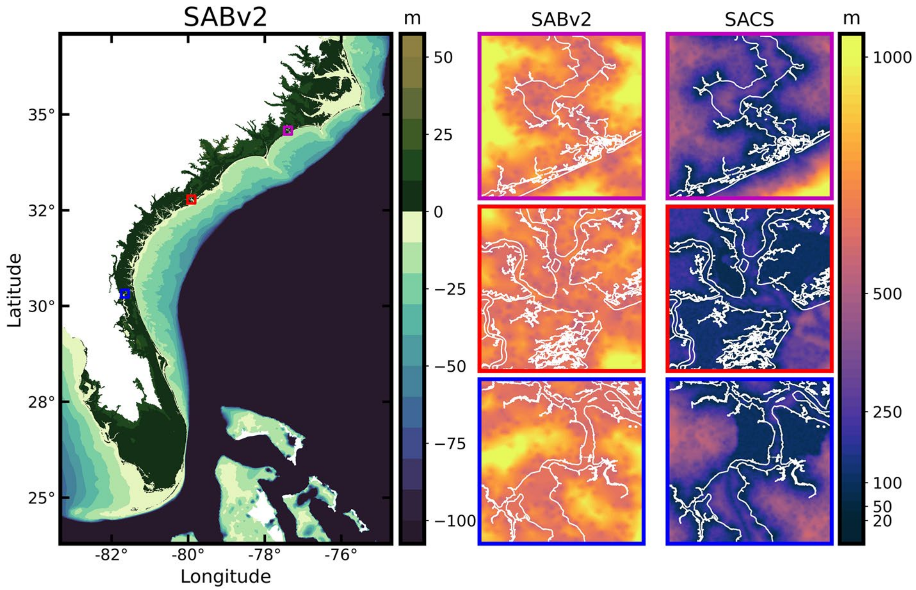

Fig. 4 SAB portions of SABv2 and SACS meshes: (left) SABv2 mesh bathymetry along the SAB, with colored boxes (magenta, red, blue) to indicate locations for (right) comparison between mesh resolutions (m) for SABv2 and SACS, with the coastline shown as a white line. Note that both the SABv2 and SACS meshes extend beyond what is shown in this figure

how the surge varied with the storm. The maximum observed storm surge in the USA during Matthew was 2.35 m above normal tide at Fort Pulaski, Georgia (GA). Similarly high water levels occurred along the SAB from Fernandina Beach, Florida (FL), Charleston, South Carolina (SC), and Hatteras, North Carolina (NC), with high water levels measuring 2.12 m, 1.89 m, and 1.85 m at these respective locations. Inundation extended inland in this region, with many locations experiencing 0.6 to 1.5 m of surge above ground level. The Racy Point gauge along the St. Johns River, FL, recorded a maximum storm tide of 1.4 m above mean higher high water (MHHW) generated by the combined effect of storm surge and freshwater input from rainfall. These flood levels varied significantly in NC with the highest levels recorded on the sound side of the Outer Banks (Stewart 2017).

2.2.4 Simulations

Wind fields and surface pressures of Matthew (2016) from Oceanweather Inc. (OWI) were used in this study to force the simulations. The OWI fields are produced from weather station, buoy, aircraft, ship, and satellite stations and are considered highly accurate for use in hurricane storm surge hindcasts (Oceanweather Inc. 2018). For Matthew, forcing data are described on a lower-resolution, basin-scale grid covering 5° N to 47° N and 99° W to 55° W with a resolution of 0.25°, and a higher-resolution, regional inset grid from 15° N to 40° N and 82° W to 68° W with resolution 0.05°. The OWI data cover a time period between 0000 UTC October 01, 2016, to 0000 UTC October 11, 2016, with a 15-minute time interval (Thomas et al. 2019).

Fig. 5 Gauge locations for Matthew (2016)

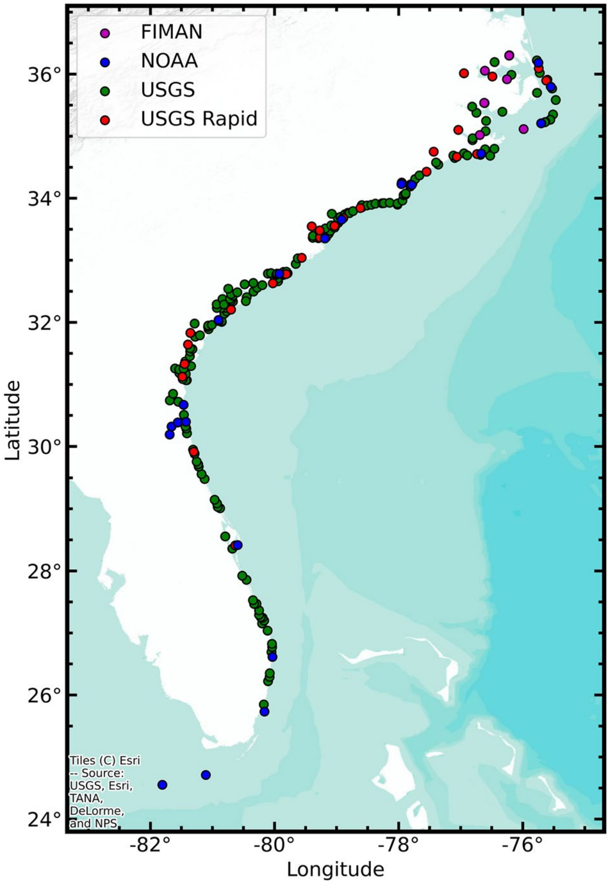

ADCIRC simulations were performed using conventional ADCIRC on both the high-resolution SACS and coarse SABv2 meshes, and subgrid ADCIRC on only the SABv2 mesh. Each simulation covered 25 days starting at 0000 UTC September 16, 2016, and ending at 0000 UTC October 11, 2016. All simulations used a 1 s timestep and started with a tidal ramp period of 5 days.

Time-dependent tidal elevation prescribed along the open ocean boundary is computed from the harmonic constituents of the TPXO tidal model (Egbert and Erofeeva 2002). For the SAB region of the SABv2 mesh, 2016 Coastal Change Analysis Program (C-CAP) regional landcover datasets were downloaded from NOAA Digital Coast (National Oceanic and Atmospheric Administration 2021a) were converted to Manning's n values (Owensby et al. 2020). Areas outside the SAB region had a constant Manning's n value of 0.02. These values were then interpolated to mesh vertices for the SABv2 coarse mesh and used for bottom friction and advection corrections in the subgrid simulation on the SABv2 mesh. Other parameters used in simulations on the SABv2 mesh included: spatially constant horizontal eddy viscosity of 50 m^2/s, variable primitive weighting coefficient (τ_0) between 0.005 and 0.03, sea surface height above geoid of 0.284 m to represent the pre-storm rise in water levels due to long-term atmospheric and oceanographic effects (Gill and Niiler 1973; Ferry and Reverdin 2000; Shin and Newman 2021), surface directional effective roughness length, and the surface canopy coefficient. The sea surface height above geoid value was determined from the mean monthly water level taken at water level gauges during the months when historical storms Hugo, Andrew, Fran, Frances, Matthew, Irma, and Florence occurred. The surface directional effective roughness and surface canopy coefficient in the SABv2 mesh were also derived from C-CAP landcover datasets and were interpolated onto the mesh using the ADCIRCModules toolkit (Cobell 2020). The SABv2 simulations use an implicit formulation to compute the complete gravity wave term, which is available in ADCIRC v55 (Pringle et al. 2021).

Simulations on the SACS mesh used seven nodal attributes including: sea surface height above the geoid, primitive weighting coefficient, Manning's n, internal tide friction, surface directional effective roughness length, advection state, and surface canopy coefficient (Owensby et al. 2020). The same sea surface height above geoid used for the SABv2 simulations was used for the SACS simulation. NOAA's 2010 30 m C-CAP landcover dataset was used for Manning's n values and surface directional effective roughness length. Primitive weighting in the continuity equation was set to 0.03 for areas immediately surrounding the coast and 0.005 elsewhere. In areas where wooded canopy was present and likely to prevent the momentum transfer of wind to the water surface, the surface stresses were disabled via surface canopy. Internal tide friction was used in deep areas with steep bathymetric gradients (shelf breaks) to partially account for dissipation from the conversion of the barotropic tides to baroclinic tides not directly considered for in barotropic ADCIRC (Owensby et al. 2020). The SACS simulations were performed with the lumped explicit formulation (Tanaka et al. 2011).

2.3 Error metrics

Water level data from the 218 gauge locations were used to evaluate the accuracy of the ADCIRC simulations (Fig. 5). The accuracy of the simulations will be evaluated relative to observations of peak water levels and hydrographs. Peak-to-peak analysis of high water levels were compared to observations including root-mean-square-error (E_{RMS}):

$$E_{\mathrm{RMS}} = \sqrt{\frac{\sum_{i=1}^{N} \left(\zeta_i - \hat{\zeta}_i\right)^2}{N}}, \tag{12}$$

coefficient of determination (R^2):

$$R^2 = 1 - \frac{\sum_{i=1}^{N} \left(\zeta_i - \hat{\zeta}_i\right)^2}{\sum_{i=1}^{N} \left(\zeta_i - \bar{\zeta}\right)^2}, \tag{13}$$

and mean normalized bias (B_{MN}):

$$B_{\mathrm{MN}} = \frac{\frac{1}{N} \sum_{i=1}^{N} \left(\hat{\zeta}_i - \zeta_i\right)}{\frac{1}{N} \sum_{i=1}^{N} \left|\zeta_i\right|} \tag{14}$$

in which N is the number of observation stations, ζ and $\hat{\zeta}$ are the water surface elevations from the observations and predictions, respectively, and $\bar{\zeta}$ is the mean water surface elevation from the observations. Another metric was best-fit slope (m in $\hat{\zeta} = m\zeta$) from a linear regression fit between peak water levels from predictions and observations. Ideal values for E_{RMS} and B_{MN} are zero, indicating a perfect match in peak water level prediction. Ideal values for R^2 and m are unity, indicating an ideal 1-to-1 match between predictions and observations. In addition to performing error metrics on high water measurements at the gauge locations, E_{RMS} and B_{MN} statistics were calculated for the entire water level hydrographs (i.e., time series) at select locations along the coast for each simulation. For the time-series analysis, in Eqs. 12-14, N denotes the number of surface elevations in the time series, and ζ_i and $\hat{\zeta}_i$ are the model and observed surface elevation at Δt_s with Δt_s being the sampling time.

Computational efficiency was quantified by comparing the minimum run times of the subgrid and conventional ADCIRC simulations on the SABv2 and SACS meshes. The ocean-scale test case was run in parallel on 256 cores contained on 4 AMD Epyc "Milan" processors, each processor has 64 cores, and each node has 2 processors with 256 GB of memory and a clock speed of 2.45 GHz. The processors are connected via an Infiniband switch in the Anvil high-performance computing cluster at Purdue University. Each simulation was run in triplicate, and the minimum wall-clock time was used for timing comparisons.

3 Results

3.1 Level 1 corrections in synthetic winding channel

The Level 1 corrections in ADCIRC will first be evaluated via simulations of controlled flow in a synthetic compound channel. This synthetic domain (Fig. 6, left) has dimensions of 120 m by 800 m, and it consists of a planar floodplain and a deeper, trapezoidal winding channel. The planar floodplain has a slope of 0.0001 m/m, and its ground surface elevations vary linearly from −1 m at the top of the domain to −1.08 m at the bottom of the domain. The channel is always 1 m deeper than its surrounding floodplain, with sloping banks that are each 5 m wide and 1 m deep and a bed that is 5 m wide. This test was designed to not include wetting and drying. Water levels are applied as boundary conditions at the top and bottom of the domain, and then discharges (through the channel and down the beach) will be compared with and without the Level 1 corrections.

Two finite-element meshes were created to represent this problem (Fig. 6, middle and right). The coarse mesh has 224 vertices and 370 elements, the high-resolution mesh has 2052 vertices and 3734 elements, and thus the high-resolution mesh has approximately 9 times more grid cells. The coarse mesh has an average element side length of 24 m, while the high-resolution mesh has element side lengths ranging from 20 m on the floodplain to 5 m in the channel. The high-resolution mesh aligns elements and vertices with the channel banks and bed to fully resolve flow. The coarse mesh was created so that interpolation of elevation data to the vertices would alias the channel. The ground surface elevations for both meshes were interpolated using linear interpolation. Bottom friction is calculated using a constant Manning's coefficient of $n = 0.02$, and the horizontal eddy viscosity is set to $E_h = 2\ \mathrm{m}^2/\mathrm{s}$.

The water surface elevations at the top and bottom boundaries are fixed to create a constant water surface gradient. The water surface gradient is the same as the bottom slope, but the flow depth above the floodplain is varied from 0.15 m to 1.5 m. The simulations are run for 10 days to achieve steady conditions. For each simulation, the total discharge is computed by integrating the discharge across the bottom boundary. The Level 1 corrections are evaluated via deviations from the 'truth' discharge from the high-resolution simulations:

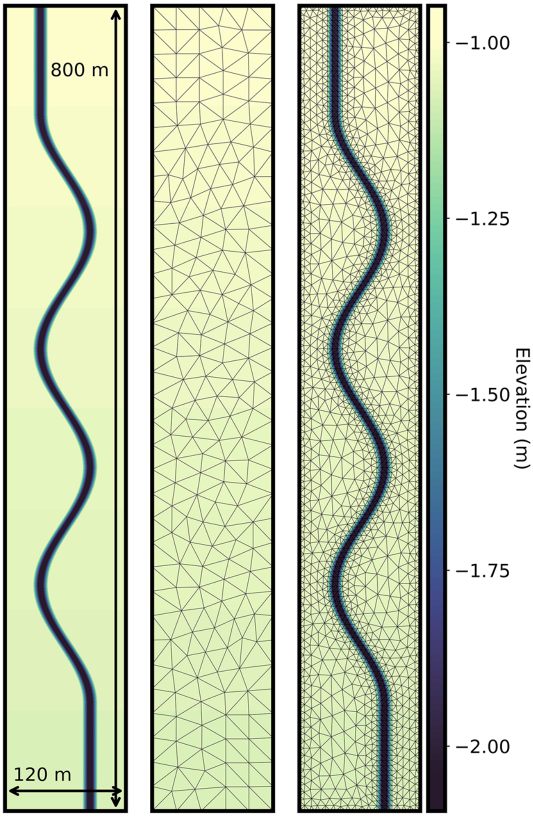

Fig. 6 From left to right, the DEM used for compound channel interpolation, coarse mesh, high-resolution mesh

$$Q_{\mathrm{dev}} = \frac{Q_{\mathrm{coarse}} - Q_{\mathrm{truth}}}{Q_{\mathrm{truth}}} \times 100\% \tag{15}$$

in which Q_{dev} is the discharge deviation (expressed as a percent difference), and Q is a discharge (units of m^3/s). Smaller deviations in discharge indicate a better representation of flow along the compound channel.

For this test case, five simulations are conducted: *High-Resolution Conventional*, in which ADCIRC is applied without any corrections on the high-resolution mesh, to provide a 'truth' solution for comparison; *Coarse Conventional*, in which ADCIRC is applied without any corrections on the coarse mesh; *Coarse Level 0*, in which subgrid ADCIRC is applied with Level 0 corrections on the coarse mesh; *Coarse Level 1 Only Advection*, where only the Level 1 correction to advection is added; and *Coarse Level 1*, in which subgrid ADCIRC is applied with Level 1 corrections on the coarse mesh. For small depths, where friction forces dominate, it is expected that the Level 0 corrections will overestimate bottom friction and thus limit artificially the total discharge. The Level 1 corrections to bottom friction, on the other hand, should be a better representation of flow processes. However, as water depths increase, the improvements offered by corrections to bottom friction should diminish as frictional effects reduce, and will give way to the corrections to advection.

All simulations under-predict discharge across the bottom boundary of the domain, when compared to a reference simulation on a high-resolution mesh (Fig. 7). The under-predictions are worse at small water depths; at a depth of 0.15 m, *Coarse Conventional* has $Q_{\mathrm{dev}} = -25.6\%$, the *Coarse Level 0* has $Q_{\mathrm{dev}} = -17.7\%$, and the *Coarse Level 1 Only Advection* has $Q_{\mathrm{dev}} = -17.6\%$. These results indicate that the bottom friction is limiting the flows predicted on the coarse mesh. This effect is reduced for *Coarse Level 1*, which has smaller discharge deviations for all water depths, notably $Q_{\mathrm{dev}} = -14.9\%$ at a water depth of 0.15 m. Therefore, at small water depths, Level 1 corrections offer improvement to simulated flow, and this improvement can mainly be attributed to enhancements in bottom friction representation.

As water depths increase, the contribution of the advection correction begins to develop. For instance, the percent difference in velocity magnitude at a water depth of 0.5 m above the floodplain shows the relative contribution of each Level 1 correction to the flow when compared to the Level 0 simulation (Fig. 8). Here, a positive percent difference (colored red) indicates a higher velocity magnitude in the Level 1 simulations. From Fig. 8, it can be seen that although the bottom friction correction dominates along the channel, the advection correction influences flow where there are abrupt changes in the channel direction.

As water depths increase further, the improvements to discharge predictions offered by Level 1 corrections begin to be dominated by the corrections to advection. At a water depth of 1.5 m, the *Coarse Level 1 Only Advection* and the *Coarse Level 1* simulations only differ by 0.43% with discharge deviations of −2.76% and −2.33%, respectively. These results

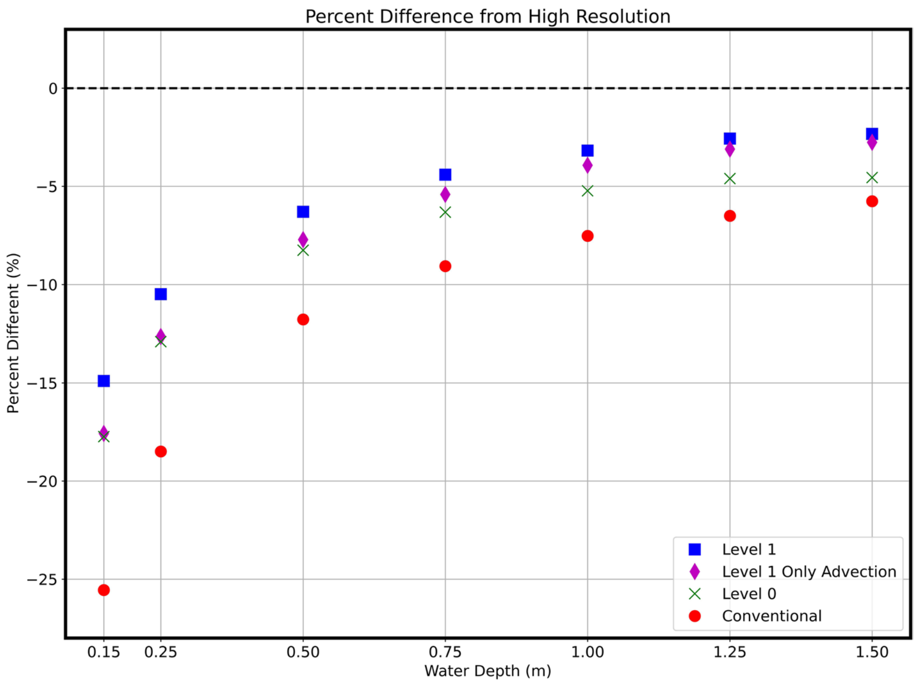

Fig. 7 Discharge deviation of the *Coarse Conventional* (red circle), *Coarse Level 0* (green X), *Coarse Level 1 Only Advection* (magenta diamond), and *Coarse Level 1* (blue square) from the high-resolution simulation (dashed line)

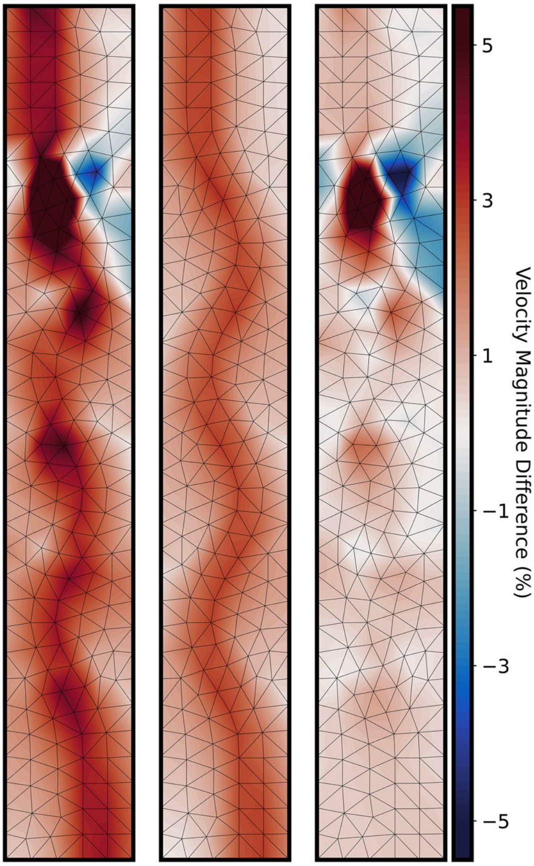

Fig. 8 Percent differences of velocity magnitudes between Level 1 and Level 0 (left), Level 1 and Level 1 Only Advection (center), and Level 1 Only Advection and Level 0 (right) at a water level of 0.5 m above the floodplain

indicate that Level 1 corrections to advection can be non-negligible and can still offer improvements to simulated flow.

3.2 Storm surge predictions in the South Atlantic Bight

Ocean-scale simulations are performed on coarse SABv2 and high-resolution SACS meshes of the Western North Atlantic with an emphasis on the SAB. Three simulations are performed: *SACS Conventional*, *SABv2 Conventional*, and *SABv2 Subgrid* with Level 1 corrections. Water levels predicted with tidal and atmospheric forcing from Matthew in 2016 are compared against observations of water levels for a 25-day period surrounding the storm.

Matthew affected water levels along the SAB from FL through NC (Fig. 9). Beginning October 7, the storm moved north from the Bahamas and started influencing water levels along the south FL coast. In this area, high water levels of 1.75 m are predicted along barrier islands and inland waterways and estuaries. High water levels of 3 m in the small canals that line the eastern FL coast are predicted in *SACS Conventional* and *SABv2 Subgrid*. Matthew continued north, steered closer to the coast throughout October 7, and began affecting the Georgia/South Carolina coast on October 8. The GA and SC coasts have

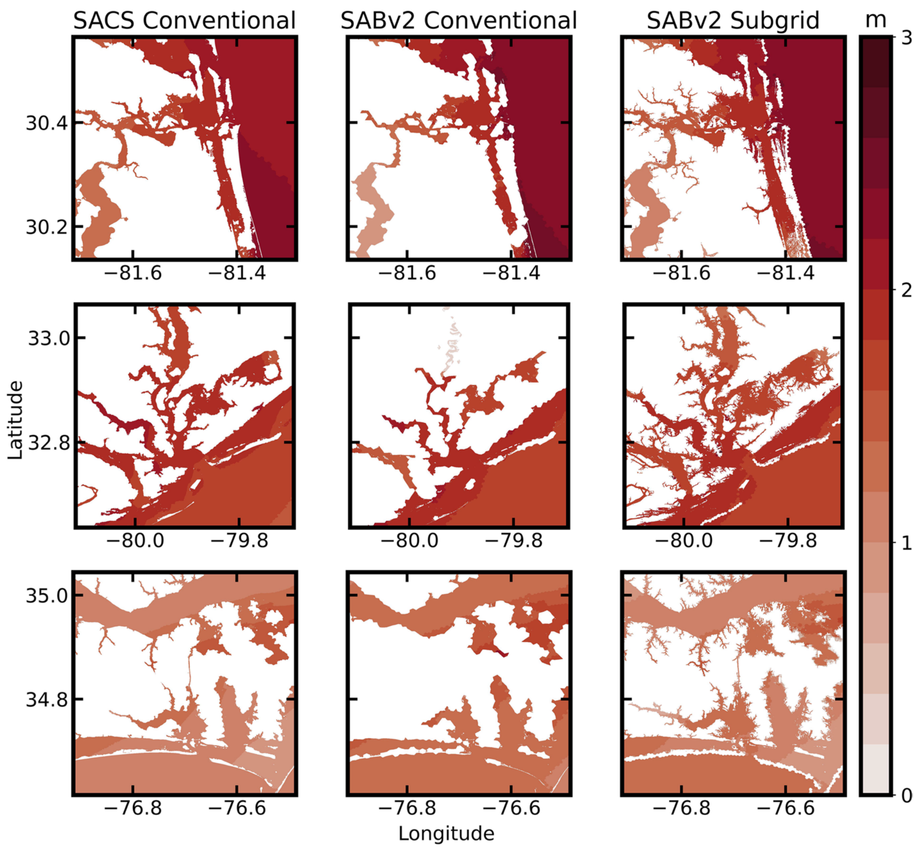

Fig. 9 Maximum water levels in the *SACS Conventional* (left), *SABv2 Conventional* (middle), and *SABv2 Subgrid* (right) simulations along the SAB as Matthew moved up the coast. From the top row to the bottom row, the locations pictured are in the regions surrounding Jacksonville, FL, Charleston, SC, and Carteret County, NC

riverine delta systems with streams, channels, and tributaries that experienced elevated water levels of about 3 m as the storm passed. Matthew tracked parallel to the coastline and caused flooding in NC on the morning of October 9 before moving offshore of the NC Outer Banks later that afternoon. Much like FL, the NC coast is characterized by barrier island and lagoon systems. As Matthew approached, storm surge was driven through tidal inlets and affected locations several kilometers from the open coast, with water levels of over 1.5 m in the Neuse River estuary. For a more detailed description of the storm's synoptic history, refer to Thomas et al. (2019).

Matthew's effects on coastal water levels were observed at 232 stations and gauges throughout the SAB. Of these 232 stations, 218 were used for water level analysis. To evaluate the performance of subgrid ADCIRC, we focus on 6 stations with representative results (Fig. 10). Most of these 6 stations were located along inland waterways and far from the open coast, to highlight the subgrid ADCIRC's ability to represent surge propagation to inland areas on a coarsened computational mesh.

Storm surge gauge FLMAR03742 (last row in Fig. 10) was located along a 40-m-wide canal near the Saint Lucie Inlet, FL. A peak water level of 0.84 m at 0441 GMT October

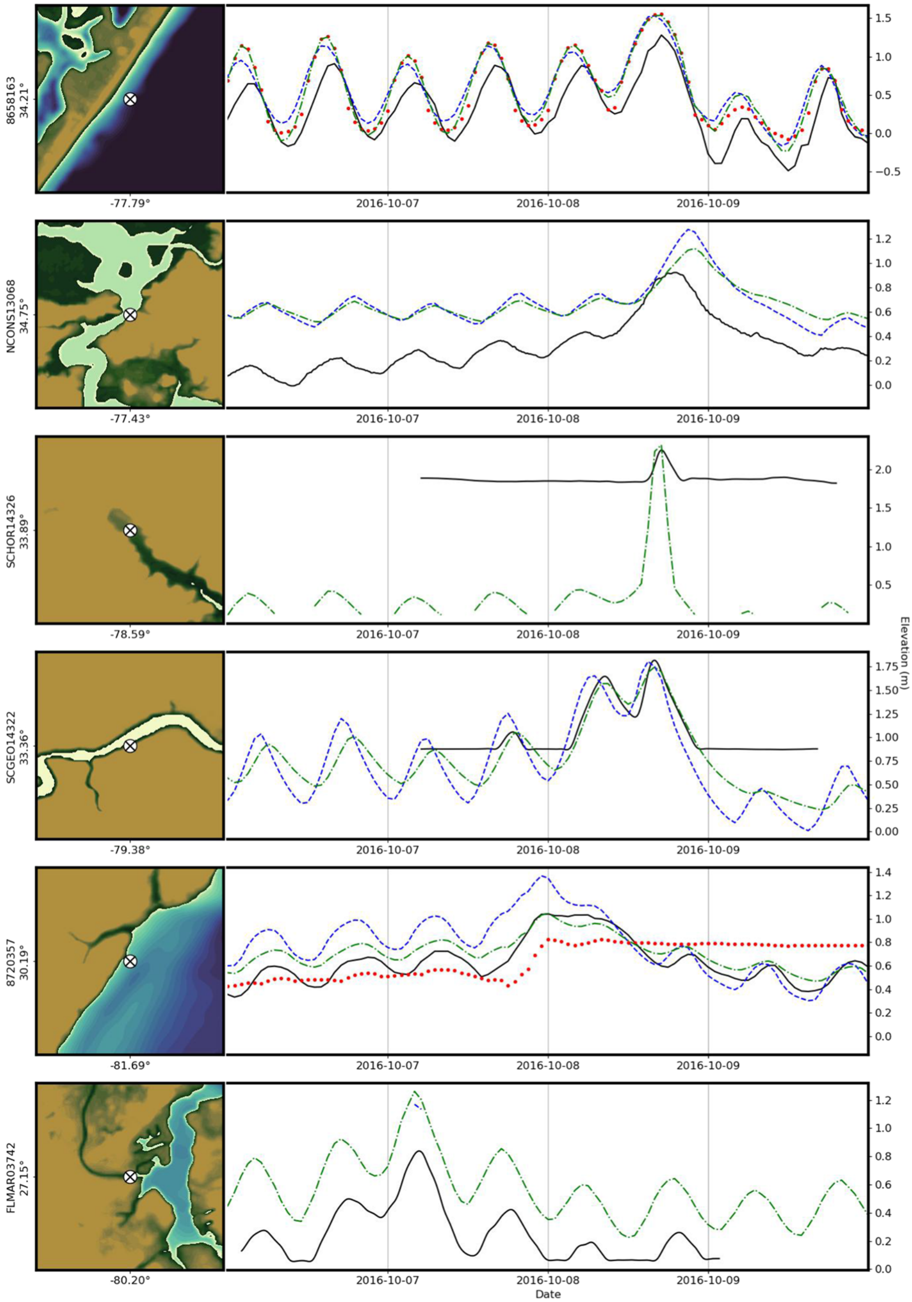

Fig. 10 Station location (left) and hydrograph comparisons (right) between observation (black solid), coarse subgrid (green dash dot), coarse conventional (red dot), SACS conventional simulations (blue dash) relative to NAVD88 datum. These stations are in order from North to South, starting on the top row with station 8658163 in Wrightsville Beach, NC and ending on the last row with station FLMAR03742 in southeast Florida

07, 2016, was observed at this gauge during the storm. In this area, the SACS mesh has 103-m resolution, and the SABv2 mesh has 775-m resolution. (Mesh resolutions at station and gauge locations were determined from element edge lengths connected to the nearest mesh vertex.) *SABv2 Conventional* was unable to resolve water levels at this station due to insufficient resolution in the surrounding area. *SABv2 Subgrid* predicted a peak water level of 1.26 m at 0400 GMT October 7, 2016, which is an over-prediction of 0.42 m. *SACS Conventional* briefly became wet at this location and recorded a peak water level of 1.17 m at 0400 GMT October 7, 2016, over-predicting the observations by 0.33 m. Although the *SACS Conventional* was able to simulate high water levels for a couple of hours surrounding the peak of the surge event, *SABv2 Subgrid* captures flow in this canal and thus had much better hydraulic connectivity in the area. Therefore, this location is an example of how subgrid corrections can improve connectivity without costly mesh refinements. In addition, *SABv2 Subgrid* had a comparable prediction error to the *SACS Conventional* at this location (Table 1).

NOAA station 8720357 (fifth row in Fig. 10) is located on the St. Johns River near the I-295 Buckman Bridge in FL. At this station, the maximum observed water level during Matthew was 1.04 m at 0000 GMT October 8, 2016. The St. Johns River in this location is nearly 5 km wide and is resolved by the SABv2 and SACS meshes with local resolutions of 674 m and 106 m, respectively. *SACS Conventional* predicted a maximum elevation of 1.37 m at 2300 GMT October 7, 2016, and over-predicted water levels at this location by 0.33 m. *SABv2 Conventional* experienced a rapid flooding event during the storm that increased water levels to 0.83 m. This water then became trapped and could not drain back to the ocean due to insufficient mesh resolution at a 350 m wide channel constriction approximately 15 km downstream on the St. Johns River toward the coast. *SABv2 Subgrid* predicted a peak water level of 1.05 m at 0000 GMT October 8, 2016, over-predicting the peak observation by 0.01 m. Therefore, although local resolution in the SABv2 mesh was sufficient to predict water levels along a wider section of the St. John's River, subgrid corrections were necessary to resolve tidal propagation and storm surge from the open coast to the station. This was also indicated by reductions in both E_{RMS} and B_{MN} at this station in the *SABv2 Subgrid* simulation.

Gauge SCGEO14322 (fourth row in Fig. 10) was placed along a 175 m-wide section of the Sampit River in Georgetown County, SC. The station was mounted at 0.88 m NAVD88 and thus could not observe the full tidal range leading up to the storm. This station recorded a peak water surface elevation of 1.82 m at 1557 GMT October 8, 2016. Mesh

Table 1 Error statistics comparing coarse and fine simulation hydrographs to observations during Matthew (2016)

Station	SACS conventional		SABv2 conventional		SABv2 subgrid	
	E_{RMS}(m)	Bias	E_{RMS}(m)	Bias	E_{RMS}(m)	Bias
8658163	0.33	0.5821	0.33	0.5745	0.33	0.5253
NCONS13068	0.35	0.9257	–	–	0.35	0.9402
SCHOR14326	–	–	–	–	0.88	− 0.2559
SCGEO14322	0.20	0.0083	–	–	0.08	0.0016
8720357	0.24	0.4369	0.21	0.2679	0.21	0.3872
FLMAR037421	0.33	0.4002	–	–	0.40	1.2167

resolutions in this area vary from 666 m in the SABv2 mesh to 100 m in the SACS mesh. At this station, both *SACS Conventional* and *SABv2 Subgrid* were able to resolve storm-induced flows in this channel. However, due to insufficient local resolution in its mesh, *SABv2 Conventional* was unable to resolve flow. *SACS Conventional* predicted a maximum water level of 1.80 m at 1500 GMT October 8, 2016, within 0.02 m of the observed peak. *SABv2 Subgrid* predicted a peak of 1.74 m at 1600 GMT October 8, 2016, or within 0.08 m of the observed peak. Although both the *SACS Conventional* and *SABv2 Conventional* predicted water levels very close to the observed peak, the subgrid simulation produced better overall results with around a third of the E_{RMS} and smaller value B_{MN}. This gauge location was chosen because it offered a direct comparison of results produced by the high-resolution SACS mesh and the coarse SABv2 mesh with subgrid corrections. Without the added corrections, the SABv2 mesh was unable to resolve flow.

Gauge SCHOR14326 (third row in Fig. 10) was located on a very small tidal creek near the border between NC and SC. SCHOR14326 recorded a maximum water surface elevation of 2.25 m at 1702 GMT October 8, 2016. This gauge was mounted at an elevation of 1.83 m NAVD88, and thus could not measure the tidal fluctuations leading up to the storm. The tidal creek has a width of less than 2 m. The resolution surrounding this location is roughly 663 m and 255 m in the SABv2 and SACS meshes, respectively. At this gauge, only *SABv2 Subgrid* can represent flow, neither *SACS Conventional* nor *SABv2 Conventional* have the necessary resolution to resolve this small-scale channel. *SABv2 Subgrid* predicted a peak water level of 2.31 m at 1700 GMT October 8, 2016, which was within 0.06 m of the observed peak. The small channel near the gauge would be difficult to resolve in an ocean-scale model, because the resolution required would be expensive with respect to simulation wall-clock time.

Gauge NCONS13068 (second row in Fig. 10) was located near Jacksonville, NC, along the New River adjacent to Camp LeJeune Marine Base. Station NCONS13068 recorded a maximum water surface elevation during the storm of 0.92 m at 1854 GMT October 8, 2016. The SABv2 and SACS meshes have resolution in this area of 625 m and 56 m, respectively. The New River is connected to the Atlantic Ocean through a channel that is 250 m wide, and the channel surrounding the gauge location is 100 m wide. Thus, storm surge and tidal propagation to the gauge cannot be simulated with the SABv2 mesh due to insufficient resolution. This is evident in the hydrograph, where *SABv2 Conventional* does not show any water level results for the location. The coarse subgrid and SACS simulations are able to resolve flow though the New River estuary. *SABv2 Subgrid* predicted a maximum water level at the station of 1.12 m at 2200 GMT October 8, 2016 and *SACS Conventional* had a result of 1.27 m at 2100 GMT October 8, 2016.

NOAA station 8658163 (top row in Fig. 10) is located at the end of the Johnnie Mercers Fishing Pier in Wrightsville Beach, NC. At this location, the maximum observed water level reached 1.28 m at 1700 GMT October 8, 2016. This sensor is located along the open coast and was exposed to unobstructed tides and surge during Matthew. At this location, the SABv2 mesh has resolution of 760 m, whereas the SACS mesh has resolution of 130 m. At the open coast, this resolution should be sufficient to fully resolve flow. All of the simulations predicted water levels at this location, with *SABv2 Subgrid* predicting 1.54 m at 1700 GMT October 8, 2016, *SACS Conventional* predicting 1.53 m at 1600 GMT October 8, 2016, and *SABv2 Conventional* predicting 1.56 m at 1700 GMT October 8, 2016.

Maximum water levels from simulations were compared to observations across the SAB using 1:1 plots (Fig. 11), E_{RMS}, R^2, B_{MN}, number of dry stations, and best-fit slope (Table 2) to evaluate the performance of each simulation at predicting peak water levels. When considering all 218 high water levels, *SABv2 Subgrid* out-performed both *SABv2 Conventional*

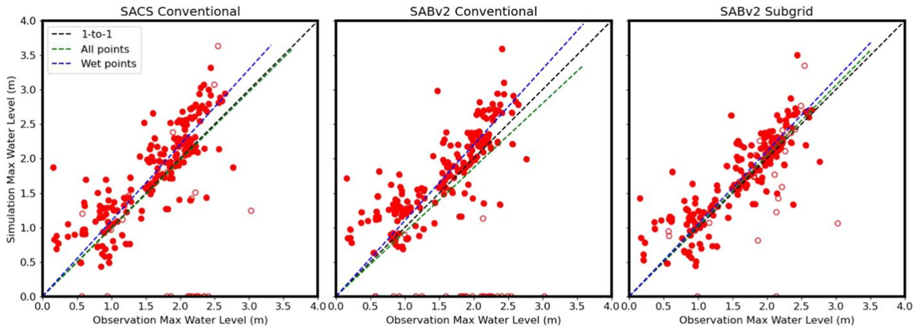

Fig. 11 Peak water level comparison between observations and simulations for *SACS Conventional*, *SABv2 Conventional*, and *SABv2 Subgrid* in relation to NAVD88 datum. The green line in the plots represents the linear regression best fit for all of the stations, the blue line represents the linear regression best fit for only the wet stations in the simulation. The solid red dots represent observation stations that were wet in all simulations, and the empty dots represent observation comparison for the particular simulation

Table 2 Statistics from peak-to-peak analysis of subgrid and non-subgrid simulations when compared to observational data taken during Matthew (2016)

Simulation	E_{RMS} (m)	R^2	Best fit slope (m/m)	B_{MN}	Dry stations
SACS conventional all stations	0.67	– 0.13	0.99	0.0316	14
SABv2 conventional all stations	0.77	– 0.52	0.93	– 0.0126	25
SABv2 subgrid all stations	0.41	0.57	1.02	0.0535	2
SACS conventional wet stations	0.41	0.56	1.1	0.1287	–
SABv2 conventional wet stations	0.43	0.53	1.10	0.1442	–
SABv2 subgrid wet stations	0.35	0.68	1.05	0.0826	–

and *SACS Conventional* across almost every error metric. Hydraulic connectivity was improved significantly in *SABv2 Subgrid*, in which only two observation locations were not wetted during the storm simulation. There was a reduction in variance (R^2) off the 1:1 line in *SABv2 Subgrid*, indicating that the accuracy of the model results were improved. *SABv2 Conventional* and *SACS Conventional* produced negative R^2 values, indicating that their predictions had a higher variance from the 1:1 than the mean of the observations. This high variance can be attributed to the large number of dry observation stations during their simulations: 14 dry stations for *SACS Conventional*, and 25 dry stations for *SABv2 Conventional*. The E_{RMS} of the peak water levels from *SABv2 Subgrid* was 47% and 39% lower than that of *SABv2 Conventional* and *SACS Conventional*, showing that there was an increase in accuracy offered by the subgrid model. Finally, the best-fit slope of *SABv2 Subgrid* shows a near-perfect fit to the observational data, meaning that the simulation and observations are highly correlated in the subgrid model.

Separately, peak water level statistics of the stations that became or remained wet in all simulations were analyzed to examine how the models predicted water levels when dry stations are not factored into calculations. Discounting the dry stations reduced peak water level prediction error (E_{RMS}) of all simulations, most notably in *SABv2 Conventional* and *SACS Conventional*, which showed a 44% and 39% improvement, respectively. *SABv2*

Subgrid showed improvements to E_{RMS} and R^2, but the simulation best-fit slope moved slightly off 1.02. The only-wet analysis also significantly increased the B_{MN} of the *SABv2 Conventional* and *SACS Conventional*, which indicates that the model consistently over-predicts water levels.

Computing times of the three models used in this study show that the subgrid additions added computational expense to the model (Table 3). When compared to conventional ADCIRC run on the same computational mesh, the subgrid model ran about 13% slower. However, the subgrid model ran over 13 times faster than the high-fidelity model and achieved comparable results. Thus, there was a significant efficiency gain by running subgrid ADCIRC on a coarsened mesh.

4 Discussion

The addition of Level 1 corrections and the expansion of subgrid ADCIRC to ocean-scale domains has resulted in considerable improvements to accuracy and efficiency of storm surge predictions when running on coarsened meshes. These improvements were demonstrated on a synthetic compound channel test case, and then implemented in a realistic storm surge simulation of Matthew in 2016 on an ocean-scale domain with emphasis on the South Atlantic Bight. In this section, we discuss the implications of the additional accuracy provided by the subgrid corrections, and the remaining challenges for future work.

Ocean-scale subgrid corrections improved hydraulic connectivity throughout the SAB region when compared to the conventional model on the given coarse mesh. As an example, for the water level predictions on the SABv2 mesh near the town of New Bern, NC (Fig. 12), the subgrid corrections capture hydraulic connectivity in the waterways surrounding the town. *SABv2 Conventional* does not predict water in the Trent River (which flows into the Neuse River and is approximately 300 m wide in this area), whereas *SABv2 Subgrid* fully inundates this waterway and smaller connected channels through the domain. The maximum water levels are predicted to be about 1.0 m at the confluence of the Trent and Neuse Rivers. This additional accuracy is important; New Bern fared relatively well during Matthew, but there was flooding due to storm surge in its downtown near the confluence.

Level 1 corrections improve subgrid ADCIRC by allowing the model to account for subgrid changes to bottom roughness and bathymetry to account for the effect of subgrid bathymetry and bottom roughness, which can affect bottom friction and advection terms.

Table 3 Wall-clock times (sec) for ADCIRC simulations on 256 CPUs, and ratios of wall-clock times. The average time of three simulations was reported

Wall-clock time (s)	
SACS conventional	82415
SABv2 conventional	5433
SABv2 subgrid	6083
Wall-clock time ratio	
SABv2 subgrid/SABv2 conventional	1.13
SACS conventional/SABv2 subgrid	13.4

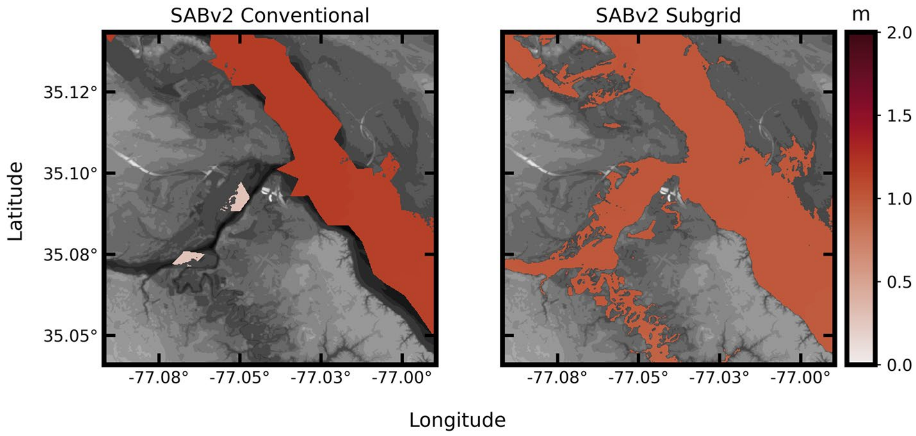

Fig. 12 Maximum water levels (m NAVD88) during Matthew for the area surrounding New Bern, NC, along the Neuse River and adjacent waterways, as predicted by *SABv2 Conventional* (left) and *SABv2 Subgrid* (right)

These additions can affect maximum storm surge height and inland penetration (Resio and Westerink 2008; Rego and Li 2010; Akbar et al. 2017; Thomas et al. 2019). The synthetic compound channel test case demonstrated that Level 1 corrections improved discharge through the channel when compared to conventional ADCIRC run on the same computational mesh, by better representing bottom friction in the model. This enhancement is important when modeling storm surge because bottom friction is often one of the main influences on inland surge propagation. The Level 1 correction to advection also influences flow by accounting for flow contractions and expansions. In the case of the New River Inlet, NC (Fig. 13), Level 1 corrections to advection increased flow velocities though the narrow inlet. This is what we would expect. As flow enters the narrow channel, it accelerates though the contraction. However, when the bathymetry of the channel is discretized onto a coarse computational mesh, the contraction is made wider and shallower and therefore will not accelerate the flow as much. By accounting for these subgrid changes in bathymetry with the Level 1 corrections to advection, we can improve the prediction of flow acceleration and velocity. In addition, the Level 1 correction to bottom friction allows flow to pass through the channel faster by reducing the bottom friction coefficient in the deeper channel. These improvements to the representation of local advection and bottom friction are a contributor to the improvements in predictive accuracy offered by the subgrid ADCIRC.

A spatially variable wetting criterion $\phi_{\min}$ was introduced into subgrid ADCIRC as a way to limit flow in regions that were hydraulically disconnected, but had elements that spanned a flow-blocking feature like a narrow barrier island. At a regional scale, this addition worked well to prevent flows from the ocean passing across barrier islands and into estuaries and other inland water ways. For example, Cape Canaveral, FL (Fig. 14, left), is characterized by a narrow barrier island (with widths as small as 100 m) and a wide lagoon. If the mesh elements are too coarse to resolve the island at the model scale, it would not act as a barrier to flows. However, with the spatially variable $\phi_{\min}$, the larger storm tides are prevented from passing from the ocean into the lagoon, at least until the island is submerged. However, this criterion is not perfect, as it can limit artificially the flows at small inlets and channels near the flow-blocking feature. In some parts of the domain, like the area surrounding Port Canaveral, FL

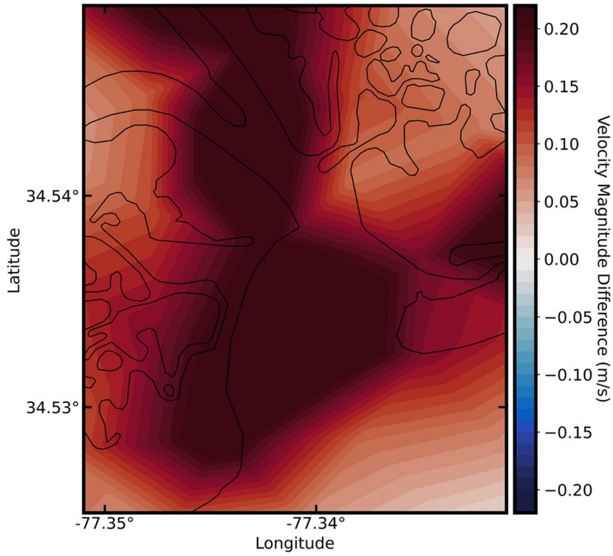

Fig. 13 Difference in velocity magnitude between *SABv2 Subgrid* simulations run with Level 1 and Level 0 corrections at the New River Inlet, NC during the height of the Matthew (2016)

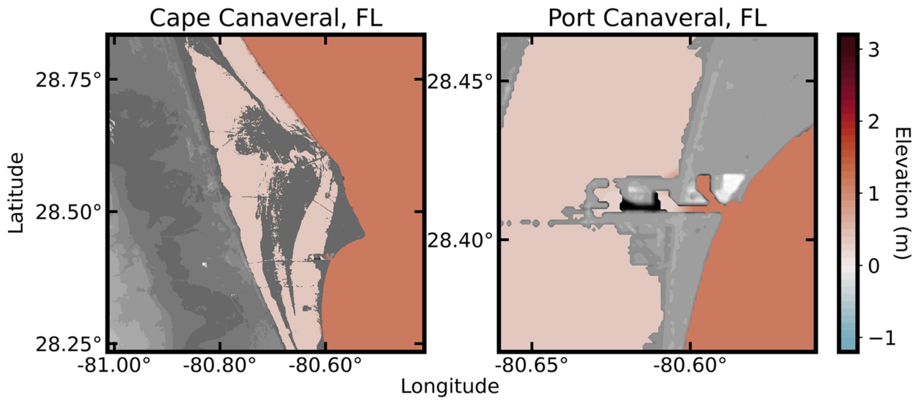

Fig. 14 Examples of flow blocking due to spatially variable $\phi_{\min}$ at 2 locations along the SAB: Cape Canaveral, FL (left) and Port Canaveral, FL (right)

(Fig. 14, right), the spatially variable $\phi_{\min}$ also inadvertently limited flow in the small channel into the port. This resulted in a lack of water level predictions from *SABv2 Subgrid* at a NOAA station 8721604 located in the port. Thus, there is need for continued improvement on the wetting and drying algorithm in subgrid ADCIRC to improve hydraulic connectivity.

5 Conclusion

In this study, higher-order subgrid corrections to advection and bottom friction were implemented in an ocean-scale storm surge model for the South Atlantic Bight. It was found that subgrid corrections allowed for accurate predictions of water levels across this domain during a simulation of Matthew in 2016 on the coarsened SABv2 computational mesh by resolving subgrid flow processes using high-resolution bathymetric and topographic data.

The main contributions and findings of this study are:

1. *The subgrid approach performs better with bottom friction and advection corrections from higher-resolution datasets.* Corrections for these processes were added to the governing equations and look-up tables. These corrections improved discharge calculations in the synthetic winding channel test case by 11% when compared to the conventional model by better representing bottom friction in the model. Advection corrections in the ocean-scale storm surge model increased flow velocity magnitudes through inlets and winding channels, allowing for better predictions of flows to inland locations.
2. *Subgrid corrections can be extended to ocean-scale domains, but only with careful design of the pre-processor to compute the corrections, the reduced representation of corrections for a range of wet area fractions, and efficient handling of corrections in memory during the simulation.* The expansion of subgrid corrections to an ocean-scale domain required extensive elevation and landcover datasets with resolution down to 1/9 arc second to cover the entire SAB. This large amount of data required the use of HPC and advanced memory management to pre-compute look-up tables and process these tables in subgrid ADCIRC.
3. *Ocean-scale subgrid corrections improved the accuracy of a hindcast storm surge simulation of Matthew in 2016 while running on a coarsened computational mesh.* Water level predictions were validated with 218 permanent and temporary station and gauge locations from south Florida to the North Carolina Outer Banks. Peak water levels and hydrographs were analyzed and showed that subgrid corrections on the SABv2 mesh produced results with 39% less error than the SACS mesh and ran over 13 times faster.

The extension of subgrid ADCIRC to ocean-scale domains has the potential to improve accuracy and reduce computational cost for forecast and design studies of hurricane storm surge. These improvements are critical when evaluating flood risk. Coastal city planners and emergency managers need to understand which areas have the highest likelihood of flooding, often with resolution to the level of critical infrastructure. This information is necessary when designing flood control structures, creating and managing evacuation routes, and making decisions during the event. However, the necessary resolution is not feasible for a conventional model, especially when trying to predict over a large region during an active storm event. Thus, subgrid corrections are a viable option for providing this information at a fraction of the computational cost of a high-resolution conventional model.

Future work may include the addition of cell clones to properly resolve flow blocking features and hydraulically disconnected elements, and changing the wetting and drying threshold to rely on grid-averaged water depth $\langle H \rangle_G$ instead of the wet area fraction ϕ. Additionally, subgrid corrections in ADCIRC could play an important role in incorporating compound flooding from rainfall into the model, because it accounts for the total wet area within a computational cell.

Author's contributions All authors contributed to the study conception and design. Material preparation, data collection and analysis were performed by JW, CD and DW. The first draft of the manuscript was written by JW, and all authors collaborated on versions of the manuscript. All authors read and approved the final manuscript.

Funding This study was supported by the National Science Foundation grants ICER 1664037 and 1664040. This work used Anvil at Purdue University through allocation MCA08X013 from the Advanced Cyberinfrastructure Coordination Ecosystem: Services and Support (ACCESS) program, which is supported by National Science Foundation Grants 2138259, 2138286, 2138307, 2137603, and 2138296. The support of the National Science Foundation is greatly appreciated by all contributors to this project.

Data availability ADCIRC is shared freely with academic researchers (https://adcirc.org). The subgrid corrections can be computed for ADCIRC with a freely available Python script (https://github.com/ccht-ncsu/subgridADCIRCUtility). Model files for the simulations in this study are available in the Data Depot at DesignSafe (https://doi.org/10.17603/ds2-0kpf-sw07).

Declarations

Conflict of interest The authors have no financial or non-financial competing interests to disclose.

References

Akbar MK, Kanjanda S, Musinguzi A (2017) Effect of bottom friction, wind drag coefficient, and meteorological forcing in hindcast of hurricane rita storm surge using SWAN + ADCIRC model. J Mar Sci Eng, 5

Atkinson LP, Menzel DW (1985) Introduction: oceanography of the Southeast United States continental shelf, vol 2. American Geophysical Union, Washington

Bacopoulos P, Hagen SC (2017) The intertidal zones of the South Atlantic Bight and their local and regional influence on astronomical tides. Ocean Modell 119:13–34

Bates PD, Hervouet JM (1999) A new method for moving-boundary hydrodynamic problems in shallow water. Proc R Soc A 455:3107–3128

Begmohammadi A, Wirasaet D, Silver Z, et al. (2021) Subgrid surface connectivity for storm surge modelling. Adv Water Res, 153

Bender C (2013) Georgia and Northeast Florida coastal storm surge and mapping study. https://fsbpa.com/2013TechPresentations/Bender.pdf, [Retrieved 23 April 2020]

Bender C (2014) East Coast Central Florida coastal storm surge and mapping study. http://www.floods.org/Files/Conf2014_ppts/E7_Bender.pdf, [Retrieved 23 April 2020]

Bender C (2015) South Florida Coastal storm surge and mapping study. http://www.floods.org/Files/Conf2015_ppts/A7_Bender.pdf, [Retrieved 23 April 2020]

Bilskie MV, Hagen SC (2013) Topographic accuracy assessment of bare earth lidar-derived unstructured meshes. Adv Water Res 52:165–177

Blain CA, Westerink JJ, Luettich RA (1994) The influence of domain size on the response characteristics of a hurricane storm surge model. J Geophy Res 99:467–479

Blain CA, Westerink JJ, Luettich RA (1998) Grid convergence studies for the prediction of hurricane storm surge. Int J Numer Methods Fluids 26:369–401

Blain CA, Cambazoglu MK, Linzell RS et al (2012) The predictability of near-coastal currents using a baroclinic unstructured grid model. Ocean Dyn. 62(3):411–437

Blanton BO, Luettich RA (2008) North Carolina Coastal flood analysis system: model grid generation. Tech Rep TR-08-05, Renaissance Computing Institute

Blanton BO, Werner FE, Seim HE et al (2004) Barotropic tides in the South Atlantic Bight. J Geophys Res 109:1–17

Blumberg AF, Mellor GL (1983) Diagnostic and prognostic numerical circulation studies of the South Atlantic bight. J Geophys Res Oceans 88:4579–4592

Bunya S, Dietrich JC, Westerink JJ et al (2010) A high-resolution coupled riverine flow, tide, wind, wind wave and storm surge model for southern Louisiana and Mississippi: Part I - Model development and validation. Monthly Weather Rev 138:345–377

Casulli V (2019) Computational grid, subgrid, and pixels. Int J Numer Methods Fluids 90:140–155

Casulli V, Stelling GS (2011) Semi-implicit subgrid modelling of three-dimensional free-surface flows. Numer Methods Fluids 67:441–449

Chen C, Zheng L, Blanton JO (1999) Physical processes controlling the formation, evolution, and perturbation of the low-salinity front in the inner shelf off the southeastern United States: A modeling study. J Geophys Res Oceans 104:1259–1288

CIRES (2014) Continuously updated digital elevation model (CUDEM)—1/9 arc-second resolution bathymetric-topographic tiles. https://coast.noaa.gov/htdata/raster2/elevation/NCEI_ninth_Topobathy_2014_8483/, accessed 15 July 2021
Cobell Z (2020) ADCIRCModules: a C++ and Python interface for manipulation of ADCIRC model data. https://github.com/zcobell/ADCIRCModules
Contreras MT, Woods B, Blakely C, et al. (2021) A channel to basin-scale unstructured grids for the US East and Gulf of Mexcico coasts. Noaa Technical Memorandum Nos CS 41
Cyriac R, Dietrich JC, Blain CA et al (2020) Wind and tide effects on the Choctawhatchee Bay plume and implications for surface transport at Destin Inlet. Regional Stud Mar Sci 35(101):131
Danielson JJ, Poppenga SK, Tyler DJ, et al. (2018) Coastal National Elevation Database: U.S. Geological Survey Fact Sheet 2018–3037
Defina A (2000) Two-dimensional shallow flow equations for partially dry areas. Water Resour Res 36:3251–3264
Dietrich JC, Kolar RL, Luettich RA (2004) Assessment of ADCIRC's wetting and drying algorithm. In: Miller CT, Farthing MW, Gray WG, et al. (eds) Proceedings of computational methods in water resources, pp 1767–1778
Dietrich JC, Bunya S, Westerink JJ et al (2010) A high-resolution coupled riverine flow, tide, wind, wind wave and storm surge model for southern Louisiana and Mississippi: Part II - Synoptic description and analysis of Hurricanes Katrina and Rita. Monthly Weather Rev 138:378–404
Dresback KM, Kolar RL, Blain CA, et al. (2010) Development and application of the coupled HYCOM and ADCIRC system. In: Proceedings of the 11th international conference, vol 388. Estuarine and Coastal Modeling, pp 259–277
Egbert GD, Erofeeva SY (2002) Efficient inverse modeling of barotropic ocean tides. J Atmos Oceanic Technol 19:183–204
Ferry N, Reverdin G (2000) Seasonal sea surface height variability in the North Atlantic Ocean. J Geophys Res 105:6307–6326
Gill AE, Niiler PP (1973) The theory of the seasonal variability in the ocean. Deep Sea Res 20:141–177
Harris DL (1963) Characteristics of the hurricane storm surge. Tech Rep Technical Paper No. 48, U.S. Department of Commerce and Weather Bureau, Washington D.C
Herdman L, Erikson L, Barnard P (2018) Storm surge propagation and flooding in small tidal rivers during events of mixed coastal and fluvial influence. J Mar Sci Eng, 6
Hope ME, Westerink JJ, Kennedy AB et al (2013) Hindcast and Validation of Hurricane Ike (2008) waves, forerunner, and storm surge. J Geophys Res Oceans 118:4424–4460
Jelesnianski CP, Chen J, Shafer WA (1992) SLOSH: sea, lake, and overland surges from hurricanes. Tech rep, U.S. Dep. of Commer., Natl. Oceanic and Atmos. Admin., Natl. Weather Serv., Silver Spring, Maryland
Kennedy AB, Wirasaet D, Begmohammadi A, et al. (2019) Subgrid theory for storm surge modeling. Ocean Modell, 144
Kerr PC, Martyr RC, Donahue AS et al (2013) US IOOS coastal and ocean modeling testbed: evaluation of tide, wave, and hurricane surge response sensitivities to mesh resolution and friction in the Gulf of Mexico. J Geophys Res Oceans 118:4633–4661
Leijnse T, van Ormondt M, Nederhoff K, et al. (2021) Modeling compound flooding in coastal systems using a computationally efficient reduced-physics solver: Including fluvial, pluvial, tidal, wind- and wave-driven processes. Coastal Eng, 163
Lin N, Emanuel KA, Smith JA, et al. (2010a) Risk assessment of hurricane storm surge for New York City. J. Geophys. Res Atmos, 115
Lin N, Smith JA, Villarini G et al (2010) Modeling extreme rainfall, winds, and surge from Hurricane Isabel (2003). Weather Forecast 25:1342–1361
Luettich RA, Westerink JJ, Scheffner NW (1992) ADCIRC: an advanced three-dimensional circulation model for shelves coasts and estuaries, report 1: Theory and methodology of ADCIRC-2DDI and ADCIRC-3DL. Tech. rep, United States Army Corps of Engineers
Medeiros SC, Hagen SC (2013) Review of wetting and drying algorithms for numerical tidal flow models. Int J Numer Methods Fluids 71:473–487
Needham HF, Keim BD, Sathiaraj D (2015) A review of tropical cyclone-generated stormsurges: global data sources, observations, and impacts. Rev Geophys 53:545–591
National Oceanic, Atmospheric Administration (2021a) Data access viewer. Retrieved 11 Oct 2021. https://coast.noaa.gov/dataviewer/#/landcover/search/
National Oceanic, Atmospheric Administration (2021b) NOAA Medium Resolution Shoreline. Retrieved 6 Oct 2021. https://shoreline.noaa.gov/data/datasheets/medres.html. Retrieved 6 Oct 2021

Oceanweather Inc. (2018) Tropical modelling. https://www.oceanweather.com/research/TropicalCyclone.html, [Retrieved 31 January 2022]
Owensby M, Bryant M, Provost L, et al. (2020) Calibration and vof the South Atlantic domain model setup for the South Atlantic coastal study (sacs). Tech rep
Pringle WJ, Wirasaet D, Suhardjo A et al (2018) Finite-element barotropic model for the Indian and Western pacific oceans: tidal model-data comparisons and sensitivities. Ocean Modell 129:13–38
Pringle WJ, Wirasaet D, Roberts KJ et al (2021) Global storm tide modeling with ADCIRC v55: unstructured mesh design and performance. Geosci Model Develop 14:1125–1145
Ramirez JA, Lichter M, Coulthard TJ et al (2016) Hyper-resolution mapping of regional storm surge and tide flooding: comparison of static and dynamic models. Nat Hazards 82:571–590
Redfield AC (1958) The influence of the continental shelf on the tides of the Atlantic coast of the United States. J Mar Resour 17:432–448
Rego JL, Li C (2010) Nonlinear terms in storm surge predictions: effect of tide and shelf geometry with case study from Hurricane Rita. J Geophys Res 115(C06):020
Resio DT, Westerink JJ (2008) Modeling of the physics of storm surges. Phys Today 69:33–38
Riverside Technology, AECOM (2015) Mesh development, tidal validation, and hindcast skill assessment of an ADCIRC model for the Hurricane Storm Surge Operational Forecast System on the US Gulf-Atlantic Coast
Roberts KJ, Pringle WJ, Westerink JJ (2019) OceanMesh2D 1.0: MATLAB-based software for two-dimensional unstructured mesh generation in coastal ocean modeling. Geosci Model Develop 12:1847–1868
Roberts KJ, Pringle WJ, Westerink JJ (2019) On the automatic and a priori design of unstructured mesh resolution for coastal ocean circulation models. Ocean Modell 144(101):509
Roberts KJ, Dietrich JC, Wirasaet D et al (2021) Dynamic load balancing for predictions of storm surge and coastal flooding. Environ Modell Softw 140(105):045. https://doi.org/10.1016/j.envsoft.2021.105045
Roig LC (1994) Hydrodynamic modeling of flows in tidal wetlands
Rucker CA, Tull N, Dietrich JC et al (2021) Downscaling of real-time coastal flooding predictions for decision support. Nat Haz 107:1341–1369. https://doi.org/10.1007/s11069-021-04634-8
Ryosuke O, Yuya U, Daisuke N, et al. (2017) Cupy: A numpy-compatible library for nvidia gpu calculations. In: Proceedings of workshop on machine learning systems (LearningSys) in the thirty-first annual conference on neural information processing systems (NIPS). http://learningsys.org/nips17/assets/papers/paper_16.pdf
Sebastian AG, Proft JM, Dietrich JC et al (2014) Characterizing hurricane storm surge behavior in Galveston Bay using the SWAN+ADCIRC model. Coast Eng 88:171–181
Sehili A, Lang G, Lippert C (2014) High-resolution subgrid models: background, grid generation, and implementation. Ocean Dyn 64:519–535
Shin SI, Newman M (2021) Seasonal predictability of global and North American Coastal sea surface temperature and height anomalies. Geophys Res Lett, 48
Stark J, Oyen TV, Meire P et al (2015) Observations of tidal and storm surge attenuation in a large tidal marsh. Limnol Oceanogr 60:1371–1381
Stewart SR (2017) Tropical cyclone report for hurricane Matthew, 28 Sept–9 Oct 2016. Tech. rep, National Hurricane Center
Tanaka S, Bunya S, Westerink JJ et al (2011) Scalability of an unstructured grid continuous Galerkin based hurricane storm surge model. J Sci Comput 46:329–358
Thomas A, Dietrich JC, Asher TG et al (2019) Influence of storm timing and forward speed on tide-surge interactions during Hurricane Matthew. Ocean Modell 137:1–19. https://doi.org/10.1016/j.ocemod.2019.03.004
Thomas A, Dietrich JC, Dawson CN, et al. (2022) Effects of model resolution and coverage of storm-driven coastal flooding predictions. J Waterway Port Coast Ocean Eng, 148
Tomiczek T, Kennedy A, Rogers S (2014) Collapse limit state fragilities of wood-framed residences from storm surge and waves during Hurricane Ike. J Waterway Port Coast Ocean Eng, 140
URS Corporation (2009) South Carolina storm surge project deliverable 1: grid development report
U.S. Army Corps of Engineers (2021) South Atlantic Coastal Study (SACS) Main Report. https://www.sad.usace.army.mil/SACS/, [Retrieved 8 July 2022]
Volp ND, van Prooijen BC, Stelling GS (2013) A finite volume approach for shallow water flow accounting for high-resolution bathymetry and roughness data. Water Resour Res 49:4126–4135
Wang HV, Loftis JD, Liu Z et al (2014) The storm surge and sub-grid inundation modeling in New York City during Hurricane Sandy. J Mar Sci Eng 2:226–246
Weaver RJ, Luettich RA (2010) 2D vs 3D storm surge sensitivity in ADCIRC: case study of Hurricane Isabel. Estuarine Coast Modell 2009:762–779

Westerink JJ, Muccino JC, Luettich RA (1992) Resolution requirements for a tidal model of the Western North Atlantic and Gulf of Mexico. In: Russell TF (ed) Computational methods in water resources, pp 669–674
Westerink JJ, Luettich RA, Muccino JC (1994) Modeling tides in the western North Atlantic using unstructured graded grids. Tellus A 46A:178–199
Westerink JJ, Luettich RA Jr, Feyen JC et al (2008) A basin to channel scale unstructured grid hurricane storm surge model applied to Southern Louisiana. Monthly Weather Rev 136:833–864
Whitacker S (1999) The method of volume averaging. Kluwer Academic Publishers, Kluwer
Woodruff J, Dietrich J, Wirasaet D, et al. (2021) Subgrid corrections in finite-element modeling of storm-driven coastal flooding. Ocean Modell, 167
Wu G, Shi F, Kirby JT et al (2016) A pre-storage, subgrid model for simulating flooding and draining processes in salt marshes. Coast Eng 108:65–78
Xian S, Lin N, Hatzikyriakou A (2015) Storm surge damage to residential areas: a quantitative analysis for Hurricane Sandy in comparison with FEMA flood map. Nat Hazards 79:1867–1888
Zhang K, Xiao C, Shen J (2008) Comparison of the CEST and SLOSH models for storm surge flooding. J Coast Res 24:489–499